

Evaluation of the Oxygen Reduction Reaction Electrocatalytic Activity of Postsynthetically Modified Covalent Organic Frameworks

Marcos Martínez-Fernández,[○] Emiliano Martínez-Periñán,[○] José I. Martínez, Marta Gordo-Lozano, Félix Zamora, José L. Segura,^{*} and Encarnación Lorenzo^{*}



Cite This: *ACS Sustainable Chem. Eng.* 2023, 11, 1763–1773



Read Online

ACCESS |



Metrics & More



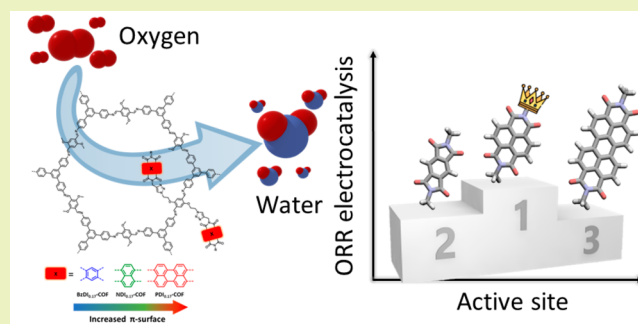
Article Recommendations



Supporting Information

ABSTRACT: The pyrolysis of organic precursors to produce heteroatomic-doped carbonaceous materials has emerged as a powerful tool to construct metal-free heterogeneous electrocatalysts due to their low cost and their environmental friendliness. However, the lack of control in the atomic positions or the location of the chemical functionalities makes it difficult to establish structure–property relationships. Herein, we report an easy strategy to compare the electrocatalytic oxygen reduction reaction (ORR) performance of metal-free and nonpyrolyzed materials by postsynthetic modification of covalent organic frameworks (COFs) via click-chemistry. This method facilitates the evaluation of different active centers using materials with the same morphology and prevents active site agglomeration by covalently anchoring these moieties inside of a porous and crystalline framework. In this study we developed a series of diimide-based materials ($\text{XDI}_{0.17}\text{-COFs}$) with a loading of 7.65×10^{-4} mol of active site/mg of host COF. The bulk COFs have been delaminated to perform electrode modification by drop-casting. The electrocatalytic response toward the ORR has been studied in alkaline media obtaining the best results for the $\text{NDI}_{0.17}\text{-COF}$ with an onset potential of 0.77 V (vs reversible hydrogen electrode, RHE) and a limiting current of 4.2 mA/cm^2 by a preferred pathway toward water electroreduction. Finally, an adequate combination of density functional theory with the thermochemical Gibbs free energy formalism has been used to theoretically rationalize the ORR mechanism in these metal-free and nonpyrolyzed materials. We have obtained theoretical ORR overpotentials for each COF system agreeing with the experimental observation, which correlate with the ability of the NDI, BzDI, and PDI molecular blocks to accommodate electrons. Our work provides a guideline on how to study the electrocatalytic performance of different organic moieties in metal-free and non-pyrolyzed COFs avoiding their de novo synthesis by using the click postsynthetic methodology.

KEYWORDS: COF, covalent organic frameworks, naphthalenediimide, electrocatalysis, oxygen reduction reaction, metal-free, pyrolysis-free



INTRODUCTION

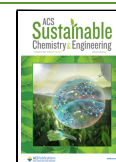
Despite the high bond energy (498 kJ/mol)¹ of the oxygen molecule, cleavage of the $\text{O}=\text{O}$ bond is an essential and highly efficient process produced in nature.^{2,3} Inspired by aerobic respiration, the oxygen reduction reaction was proposed as an ideal counter-reaction for energy conversion technologies, such as hydrogen fuel cells or metal/air batteries, due to its green nature.³ To overcome the slow kinetics of the oxygen reduction reaction (ORR),⁴ both natural and artificial $\text{O}=\text{O}$ cleavage requires the assistance of catalysts to lower the activation barrier of this process.⁵ Regarding the energy conversion technologies, even though platinum-based electrocatalysts still offer the best performances, the scarcity and the high prices of this precious metal hinder the implementation of these compounds in commercial devices.^{6,7} Different electrocatalysts have been used in the past several years, which are classified according to the pathway followed in the oxygen reduction. A two-electron reduction produces H_2O_2 as the

ORR product, while the four-electron pathway yields the direct conversion to H_2O .⁸ On one hand, the $2e^-$ reduction produces an incomplete reduction and a lower electric current, undesirable for energy conversion but interesting for hydrogen peroxide generation.⁹ On the other hand, due to the higher electric current generated by the $4e^-$ pathway and the green nature of the final product, the four-electron reduction used to be the pathway of choice in energy-related applications such as metal/air batteries.¹⁰ Several strategies have been used to control the electronic pathway followed⁹ as well as the catalyst composition in the ORR. Among them, two stand out: (i)

Received: September 28, 2022

Revised: January 7, 2023

Published: January 25, 2023



reduce the platinum load of the electrocatalyst,¹¹ and (ii) totally eliminate the Pt of the catalyst composition.^{1,3,12} Regarding the latter one, there is increasing interest in the obtainment of metal-free electrocatalysts (MFE) due to environmental reasons. Several new materials have been tested in the past few years including graphene derivatives or carbonaceous compounds, carbon nanotubes, carbon or boron nitrides, etc. Recent studies revealed that the introduction of polarized sp^2 carbon—light heteroatom (such as N, O, F, P, and S) bonds dispersed in a conductive carbon matrix creates active sites toward the ORR.^{7,13–16}

Conventional methods for the obtainment of MFE require the heteroatomic doping of carbonaceous derivatives upon treatment with reactants bearing the light heteroatoms, yielding heterogeneous distributions of these elements.¹⁷ Thus, the most widespread strategy to obtain homogeneously doped carbons is the pyrolysis of organic precursors. Among them, covalent organic frameworks (COFs) stand out among the best candidates.^{11,13,14,18} COFs are a class of polymers with superior properties such as intrinsic crystallinities, large surface areas (in some cases up to 4000 m^2/g), predesignability, and moldability of the networks which can be obtained via pre-synthetic (during the network formation) or post-synthetic (after the polymerization) approaches.^{19–21} The structure of the COFs is proposed to template the pyrolysis to homogeneously doped carbons.^{13,22} However, we envisaged that the MFE based on nonpyrolyzed COFs could produce an improvement on the performance yielded by these materials, avoiding the energetic costs associated with the pyrolytic process. Furthermore, during the pyrolytic process, the formation of the active sites is hardly controlled, and among all the functional groups produced, only some of them are the active ones.¹⁴ On the other hand, pyrolytic treatments usually lead to a loss of the porous features of the final MFEs which are highly desirable to favor the oxygen diffusion and increase the accessible active sites.^{23,24} In addition, the synthetic methods for highly crystalline COFs are often tedious,²⁵ and pyrolytic treatment causes the loss of the most noteworthy attribute of COFs, their characteristic atomic order. Thus, COF-based nonpyrolyzed MFEs have emerged as an innovative class of electrocatalysts. In this field, different organic moieties have already been incorporated into the skeleton of COFs, and some of them have been recognized as active units toward the ORR, some examples being thiophene derivatives,^{7,26} polychlorotriphenylmethyl radicals,²⁷ pyrenetetraone,²⁸ and naphthalenediimide.^{29,30} However, all of these electrocatalysts were synthesized by the de novo synthetic procedure, which is usually tedious since achieving the crystallization of a COF usually requires carrying out trial-and-error screening of the synthetic conditions which delays the evaluation of novel active units.

Here, we report an easy strategy to study different metal-free and nonpyrolyzed organic active sites and their electrocatalytic performance in the ORR of different active sites covalently anchored to the same covalent organic framework. With this aim, we have synthesized a series of porous and crystalline COFs endowed with aromatic diimides with increasing π -surfaces, i.e., benzene diimide (BzDI), naphthalenediimide (NDI), and perylenediimide (PDI), to evaluate how the electronic structure of these diimides affects the ORR performance.³¹ Thus, we decided to anchor the different moieties described by click chemistry to a well-known TAPB-DMTA-COF to obtain the series of surface-embedded

electrocatalysts ($XDI_{0.17}$ -COFs) summarized in Figure 1. By using this strategy, the COF skeleton acts as a host preventing

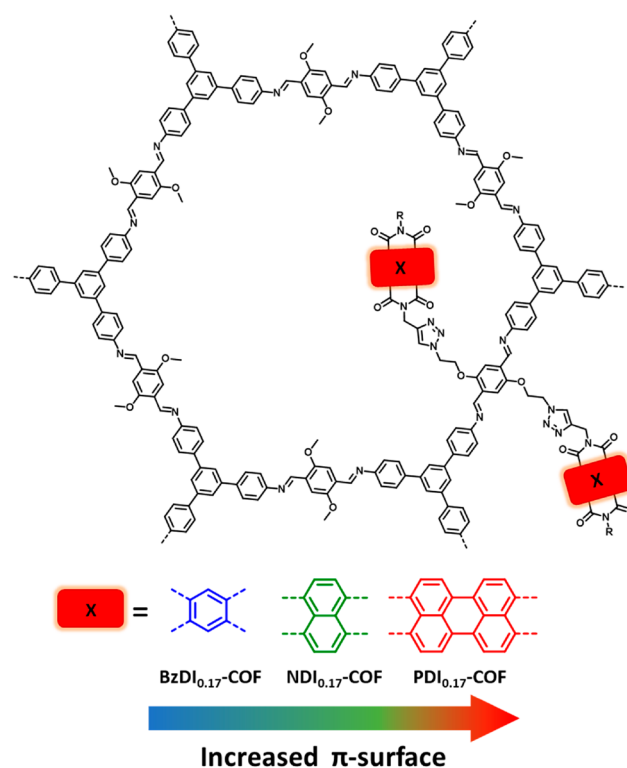


Figure 1. Schematic representation of $XDI_{0.17}$ -COFs where X represents the different π -surfaces from left to right: benzene, naphthalene, and perylene.

the agglomeration of the active units, increases the surface–volume ratio of the active units, and ensures a close contact with the electrode due to its layered macrostructure.^{32,33} The postsynthetic strategy used in this work avoids the difficulties commonly associated with the obtainment of crystalline phases in the synthesis of COFs³⁴ and facilitates the evaluation of the activity toward the ORR of different active units embedded in identical networks.

RESULTS AND DISCUSSION

Synthesis and Characterization. To anchor the different diimides by click chemistry to TAPB-DMTA-COF, we synthesized the corresponding suitably functionalized building blocks. On one hand, the synthesis of the diimides was accomplished by the imide condensation reaction between the commercial anhydrides, aliphatic amines, and 3-propargyl-amine obtaining the corresponding XDI-alkynes (Scheme 1B and Supporting Information, experimental section). On the other hand, for the modification of the COF following the postsynthetic procedure, the synthesis of the novel $Azide_{0.17}$ -COF was carried out. To address this end, a terephthalaldehyde derivative endowed with two azide functionalities (BAETA) was synthesized by a two-step synthetic procedure. The first step involves two Williamson monoetherification reactions of the previously reported dihydroxyterephthalaldehyde (DHTEA) to afford the dibrominated derivative (BBETA). The subsequent reaction with sodium azide displaces the pendant bromine electrophiles of the BBETA intermediate to yield the target BAETA (Scheme 1A). It should be noticed that, despite

Scheme 1. (A) Synthetic Route for BAETA Monomer and (B) Synthetic Route towards XDI_{0.17}-COFs^a

A) BAETA synthetic route:

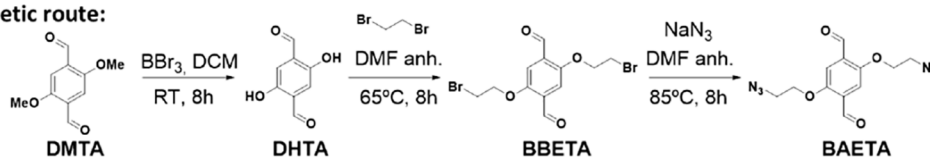
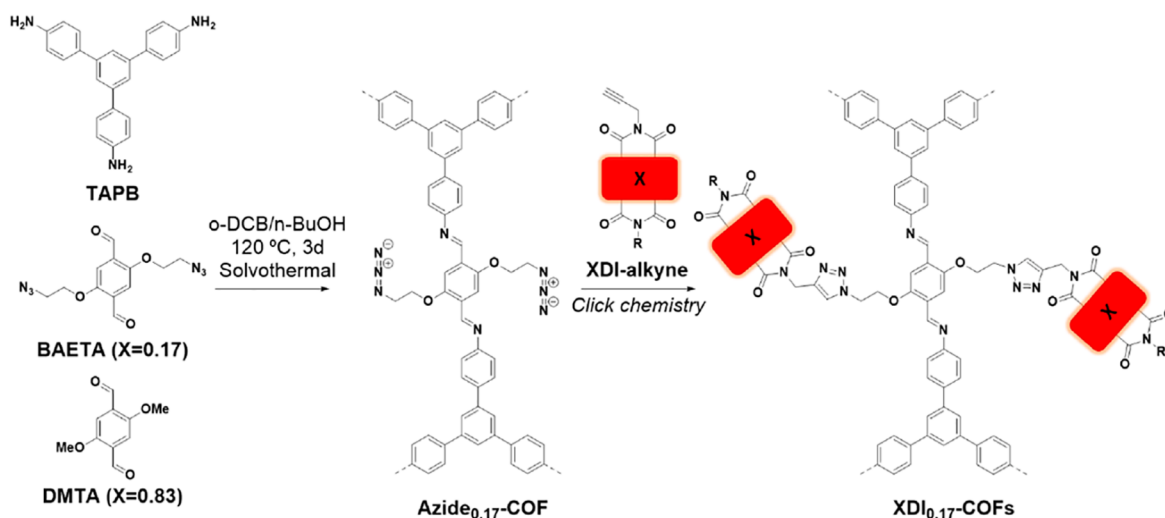
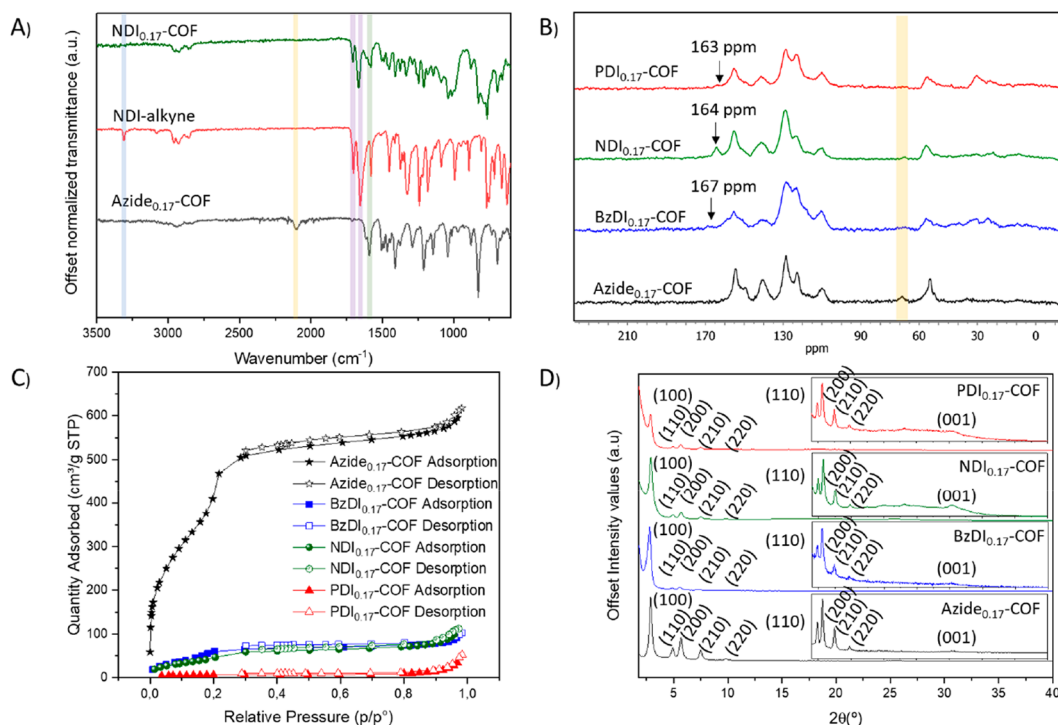
B) XDI_{0.17}-COFs synthetic route:^aThe full COF structure was omitted for clarity purposes.

Figure 2. (A) Comparison between the FTIR spectra of Azide_{0.17}-COF (black), NDI-Alkyne (red), and NDI_{0.17}-COF (alkyne disappearance highlighted in blue, azide disappearance highlighted in yellow, imide and imine retainment highlighted in purple and green, respectively). (B) ¹³C-CP-MAS NMR of Azide_{0.17}-COF (black), BzDI_{0.17}-COF (blue), NDI_{0.17}-COF (green), and PDI_{0.17}-COF (red). (C) N₂ sorption isotherms at 77 K of Azide_{0.17}-COF (black), BzDI_{0.17}-COF (blue), NDI_{0.17}-COF (green), and PDI_{0.17}-COF (red). (D) PXRD patterns of Azide_{0.17}-COF (black), BzDI_{0.17}-COF (blue), NDI_{0.17}-COF (green), and PDI_{0.17}-COF (red). Inset shows diffractogram magnification from 4° to 40°.

other azide-based COFs having been reported in the literature, this protocol allowed us to implement the azide moieties to the TAPB-DMTA-COF previously described by Jiang and co-

workers.³⁵ The main reason is that TAPB-DMTA-COF presents superior stability to hydrolysis as compared to other azide-pendant COFs based on boronate esters³⁶ or polarized

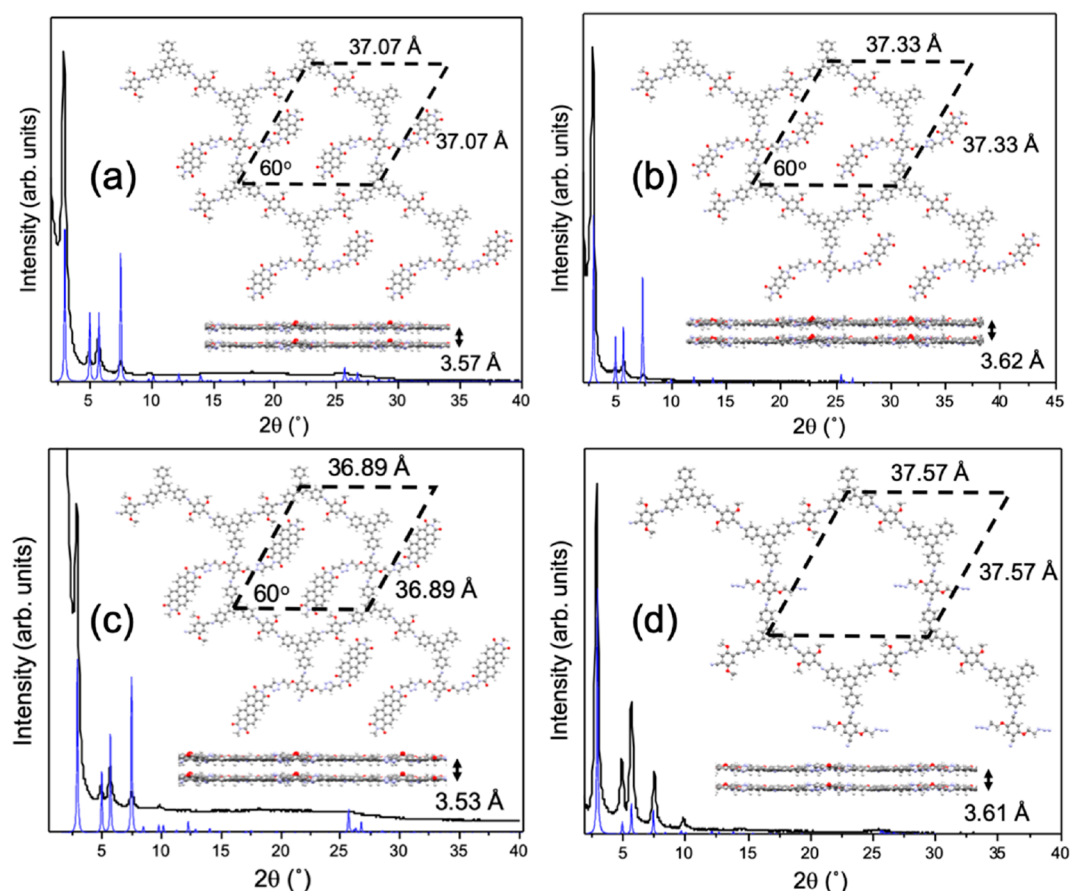


Figure 3. Comparison between the experimental and the theoretically simulated diffractograms obtained from the resulting optimized structures for (a) NDI-COF, (b) BzDI-COF, (c) PDI-COF, and (d) Azide-COF. Top and side pictorial views of the structures are also shown in each panel, indicating the resulting optimized unit cell. It is important to notice that the preferential interlamellar stacking for all the compounds is the eclipsed configuration, showing in all cases a very similar interlayer distance.

imine-linkages³⁷ which were used in the literature to anchor azide moieties and perform click postfunctionalization. We envisaged that the stability of the COF skeleton is a key feature to design electrocatalysts since the ORR experiments need to be performed in acidic or alkaline media.³ Furthermore, we decided to use a two-carbon-spacer between the azide and the ether functional groups, instead of the larger linker used by Dichtel and co-workers,³⁷ to avoid pore saturation, ensuring quantitative reaction with the terminal alkynes that are the aim of this study.

Azide_{0.17}-COF was synthesized by solvothermal reaction between TAPB, DMTA, and BAETA in a 1,2-dichlorobenzene/*n*-butanol (1/1) mixture, in a vacuum-sealed Pyrex vessel at 120 °C for 3 days (Scheme 1B). On one hand, the successful polymerization of **Azide_{0.17}-COF** was followed by Fourier transformed infrared (FTIR) spectroscopy (Figure S1) which shows the fading of the signals corresponding to the aldehyde (1667 cm⁻¹) and amine (3430 and 3350 cm⁻¹) functionalities, the retainment of the azide band (at 2100 cm⁻¹), and the emergence of the imine signal (1621 cm⁻¹).³⁸ To estimate the real azide contents, we plotted a standard curve based on the protocol described by Jiang and co-workers³⁵ by employing the characteristic stretching bands of the azide functional group around 2100 cm⁻¹ and using the BAETA monomer as equivalent for **Azide_{1.00}-COF** as the standard. In this manner, the real content was determined by interpolation of the integrated area of the FTIR spectra (in absorption) of

Azide_{0.17}-COF between 2050 and 2177 cm⁻¹, obtaining a value of 0.1643% of real azide functionalities in the COF (Figure S2), which is close to the 1/6 ratio. On the other hand, ¹³C cross-polarization magic angle spinning nuclear magnetic resonance (¹³C-CP-MAS NMR) spectra confirm the network formation by the emergence of the imine signal at 154.48 ppm.³⁹ In addition, signals from 149.5 to 109.9 ppm correspond to the aromatic fragments of the COF skeleton, while the signals at 68.5 and 54.3 ppm correspond to the alpha anisochronous carbons next to the azide and ether functionalities, respectively (Figure S3).

The synthesis of **XDI_{0.17}-COFs** was accomplished by the copper(I) catalyzed Huisgen azide-alkyne cycloaddition reaction (Scheme 1B). The progress of the heterogeneous reaction was monitored by FTIR with the disappearance of the XDI alkyne-hydrogen (≡C-H) stretching band around 3260 cm⁻¹ and the azide tension at 2100 cm⁻¹, ensuring a molar loading around 7.65 × 10⁻⁴ mol of XDI unit/mg of host COF. In addition, the signals corresponding to the nonreacting functionalities were retained. Thus, the imine band at 1621 cm⁻¹ and the imide symmetric and asymmetric stretching bands appear at 1772 and 1722 cm⁻¹ for **BzDI_{0.17}-COF**, 1706 and 1666 cm⁻¹ for **NDI_{0.17}-COF**, and 1697 and 1661 cm⁻¹ for **PDI_{0.17}-COF**, in concordance with that observed in the corresponding molecules (Figure 2A and Figures S4–S6). On the other hand, all of the solids were characterized by ¹³C-CP-MAS NMR, revealing the disappearance of the azide alpha

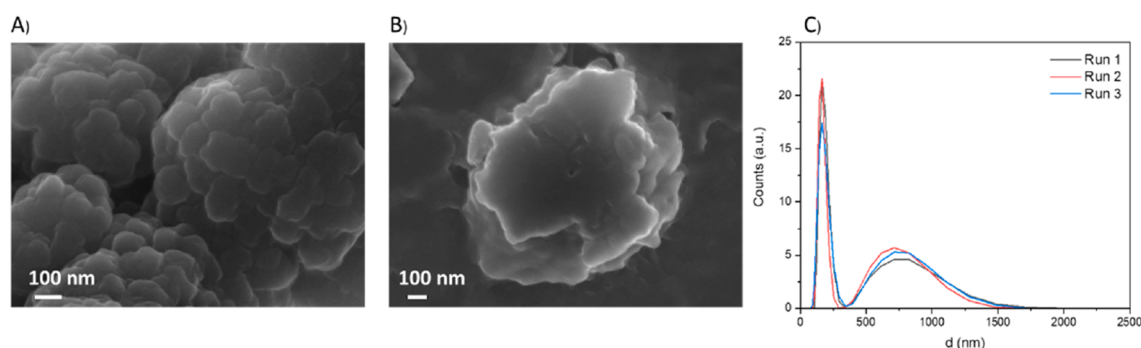


Figure 4. (A) SEM micrograph of $\text{BzDI}_{0.17}\text{-COF}$ (90,000 \times ; scale bar 100 nm). (B) SEM micrograph of $\text{BzDI}_{0.17}\text{-CONs}$ (65,000 \times ; scale bar 100 nm). (C) DLS distributions of $\text{BzDI}_{0.17}\text{-CONs}$ in water.

carbons as expected for a quantitative reaction, as well as the imide functionalities at 167, 164, and 163 ppm for $\text{BzDI}_{0.17}\text{-COF}$, $\text{NDI}_{0.17}\text{-COF}$, and $\text{PDI}_{0.17}\text{-COF}$, respectively (Figure 2B and Figures S7–S9).

The porosity of the activated materials was evaluated through the nitrogen sorption isotherms at 77 K (Figure 2C and Figures S10–S13). $\text{Azide}_{0.17}\text{-COF}$ showed a type IV isotherm revealing its mesoporous nature, in concordance with that previously reported for COFs based on the TAPB-DMTA-COF skeleton.³⁸ On the other hand, $\text{XDI}_{0.17}\text{-COFs}$ showed a reduction of the nitrogen uptake, due to the introduction of the bulky electroactive units. The Brunauer–Emmet–Teller (BET) equation was applied to the isotherms to calculate the BET surface area of the COFs (Figures S14–S17). In this way, $\text{Azide}_{0.17}\text{-COF}$ displayed 1460 $\text{m}^2 \text{g}^{-1}$ of surface area which was considerably reduced by the introduction of the electroactive units to 177 $\text{m}^2 \text{g}^{-1}$ for $\text{BzDI}_{0.17}\text{-COF}$, 158 $\text{m}^2 \text{g}^{-1}$ for $\text{NDI}_{0.17}\text{-COF}$, and 23 $\text{m}^2 \text{g}^{-1}$ for $\text{PDI}_{0.17}\text{-COF}$, in concordance with the experimental correlation found with the XDI size in the PXRD and similar experiments in the literature.⁴⁰ Furthermore, the pore volume at 0.95 p/p° also was considerably reduced after the introduction of the XDI moieties from 0.921 $\text{cm}^3 \text{g}^{-1}$ for $\text{Azide}_{0.17}\text{-COF}$ to 0.142, 0.153, and 0.028 $\text{cm}^3 \text{g}^{-1}$ for $\text{BzDI}_{0.17}\text{-COF}$, $\text{NDI}_{0.17}\text{-COF}$, and $\text{PDI}_{0.17}\text{-COF}$, respectively. Likewise, the pore size distribution was reduced from 3.2 to 2.3 nm ($\text{BzDI}_{0.17}\text{-COF}$), 2.0 nm ($\text{NDI}_{0.17}\text{-COF}$), and 1.7 nm ($\text{PDI}_{0.17}\text{-COF}$) (Figures S18–S21).

The powder X-ray diffraction (PXRD) technique was used to analyze the crystalline nature of all of the samples (Figure 2D and Figures S22–S25). First, $\text{Azide}_{0.17}\text{-COF}$ presents 6 prominent diffraction maxima which correspond to the diffraction pattern of the parent TAPB-DMTA-COF previously described by Jiang and co-workers.³⁵ The diffraction maxima centered at 2.9 $^\circ$ correspond to the (100) diffraction plane, while the diffraction maxima registered at 4.9 $^\circ$, 5.7 $^\circ$, 7.4 $^\circ$, 13.7 $^\circ$, and 25.4 $^\circ$ can be assigned to (110), (200), (210), (220), and (001) reflections. A large battery of DFT-based calculations was carried out by using an adequate combination of the Gaussian 16⁴¹ and QUANTUM ESPRESSO⁴² software packages to solve the crystalline structure of the different $\text{XDI}_{0.17}\text{-COFs}$ as well as the $\text{Azide}_{0.17}\text{-COF}$ within the present study (see further details on computational details in the SI, Section S1). Results of these simulations reveal that all of the crystal structures exhibit a purely hexagonal symmetry with lattice parameters of the monolayers ranging between 36.9 and 37.6 Å. In all cases, the preferred stacking configuration is the

eclipsed one showing very similar interlayer distances ranging between 3.53 and 3.62 Å (Figure 3). Theoretically simulated diffractograms on the basis of the optimized crystal structures of Figure 3 show an excellent agreement with the experimental ones, mimicking even the high-angle features directly related with the preferred AA packing fashion and interlayer distances, which reinforce the validity of the structures obtained by the simultaneous structure + cell DFT geometrical optimizations. These values were corroborated by performing Pawley refinement by using GSAS-II⁴³ software (Figure S26), of which lattice parameters (Table S1) show negligible differences which those exposed previously. Finally, these results are in good agreement with those reported in the literature for the postmodification of the original COF with different moieties.^{40,44,45} As expected, postsynthetic modification via Huisgen reaction does not produce a displacement of these diffraction maxima, confirming that the COF lattice remains unaltered after postfunctionalization. However, the introduction of the diimide moieties produces a gradual reduction of intensity of the diffraction maxima proportionally to the sizes of the unit introduced in the pores.^{40,44,45} Thus, these $\text{XDI}_{0.17}\text{-COFs}$ could be considered as an organized pattern of the TAPB-DMTA-COF embedding electroactive moieties covalently anchored to the pore walls with random orientations.

Thermal stabilities of the $\text{XDI}_{0.17}\text{-COFs}$ were tested through thermogravimetric analysis (TGA) (Figures S27–S29). Thermograms of $\text{BzDI}_{0.17}\text{-COF}$ and $\text{NDI}_{0.17}\text{-COF}$ revealed a weight loss of 24% at around 380 $^\circ\text{C}$ and showed a progressive mass decrease of 15% until 700 $^\circ\text{C}$ according to the degradation of the COF skeleton.⁴⁴ Meanwhile, $\text{PDI}_{0.17}\text{-COF}$ displayed three weight losses at around 252 $^\circ\text{C}$ (4%) and 425 $^\circ\text{C}$ (21%) which corresponds to the degradation of the long aliphatic chains that bear PDI⁴⁶ and the COF network, respectively. Finally, a mass decrease of 12% was observed until 700 $^\circ\text{C}$ according to the previous reported literature.⁴⁴

The morphologies of the products were studied through surface electron microscopy (SEM) in a JEOL 7600F microscope. SEM micrographs showed a polygranular rodlike composition for the $\text{Azide}_{0.17}\text{-COF}$, revealing that the morphology of the COF remains unaltered from the TAPB-DMTA-COF by introducing the azide moiety as an anchoring point (Figure S30). Furthermore, after the click postfunctionalization, the $\text{XDI}_{0.17}\text{-COF}$ retains the rodlike macrostructure of the parent $\text{Azide}_{0.17}\text{-COF}$, manifesting the “soft” behavior of Huisgen’s reaction during the postsynthetic modification of the COF materials (Figure 4A and Figures S31–S33). These morphologies seem suitable to properly delaminate the COF’s

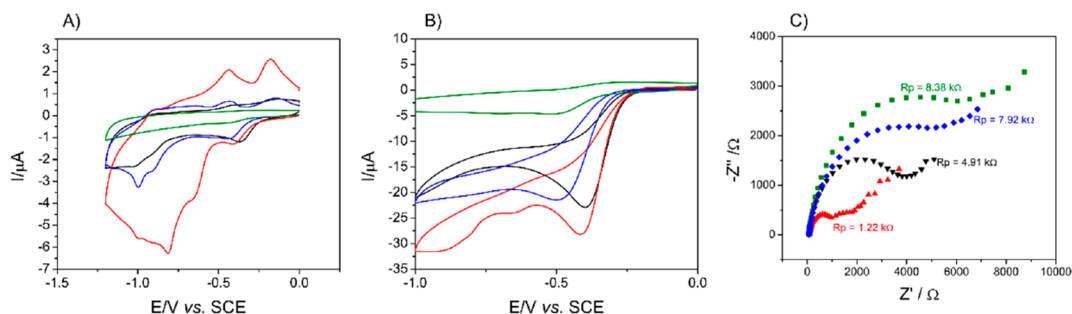


Figure 5. Cyclic voltammograms of bare Carbon SuperP/GC (green) and modification with BzDI_{0.17}-COF (black), NDI_{0.17}-COF (red), and PDI_{0.17}-COF (blue) in a 0.1 M NaOH solution (A) in the absence and (B) in the presence of saturated O₂ at 10 mV/s. (C) Nyquist plot obtained from EIS experiments using bare Carbon SuperP/GC (green) and modification with BzDI_{0.17}-COF (black), NDI_{0.17}-COF (red), and PDI_{0.17}-COF (blue) in an O₂ saturated 0.1 M NaOH solution ($E_{app} = -0.4$ V vs SCE).

layered nanostructure into covalent organic nanosheets (also known as CONs)⁴⁷ and allow the electrode modification for the ORR electrocatalysis experiments via drop-casting. In this way, 1 mg of XDI_{0.17}-COFs was introduced in commercial 20 mL glass vials and suspended in 5 mL of THF/H₂O (7/3) mixture, acidulated with 5.5 μ L of HCl (36%) and subduced in an ultrasonic bath (35 kHz and 80 W) for 30 min. The nonexfoliated material was pulled apart via ultracentrifugation at 6000 rpm for 45 min, and the colloidal XDI_{0.17}-CONs were collected from the supernatant using a glass pipet. The colloidal nature of the obtained suspension was corroborated by the Tyndall effect upon irradiation with a laser beam. SEM micrographs revealed the layered morphology of the XDI_{0.17}-CONs, a consequence of the disruption of the noncovalent interactions between the COF layers (Figure 4B and Figures S34–S36). Furthermore, heterogeneous distributions of sizes and shapes were observed for all products. Transmission electron microscopy (TEM) revealed the thin structure of the obtained XDI_{0.17}-CONs (Figures S37–S39). Finally, dynamic light scattering (DLS) was employed to measure the hydrodynamic sizes of the colloidal XDI_{0.17}-CONs, obtaining a bimodal distribution centered around 260 and 950 nm for the three products (Figure 4C and Figures S40–S42), in concordance with the experimental evidence found in electronic microscopy.

For the electrochemical measurements, 1 mg of XDI_{0.17}-COFs and 1 mg of conductive Carbon SuperP in 1 mL of a mixture of EtOH/H₂O (7/3) acidulated with 5.5 μ L of HCl (36%) were suspended using an ultrasonic bath (45 kHz and 80 W) for 60 min. A GC electrode was modified with the obtained suspensions by drop-casting. The electrochemical behavior of XDI_{0.17}-COFs/Carbon SuperP/GC was studied by cyclic voltammetry in basic medium (0.1 M NaOH) in the absence of oxygen (Figure 5A) and compared to that of Carbon SuperP/GC. As can be observed, for the three XDI_{0.17}-COFs under study, two main quasireversible redox pairs appear at $E_{1,red} = -0.42$ V/ $E_{1,ox} = -0.15$ V vs SCE and $E_{2,red} = -1.00$ V/ $E_{2,ox} = -0.47$ V vs SCE. According to the literature, both redox processes are ascribed to the reversible enolation of carbonyl groups of diimides.^{48,49} Slight potential variations and important current intensity differences are detected among the electroactive groups under study (BzDI, NDI, and PDI) as a consequence of the different π -surface of the structure. NDI_{0.17}-COF presents the higher current intensity (see Figure 5A, red curve), which indicates that the redox process is favored in comparison with those observed for PDI_{0.17}-COF (see Figure 5A, blue curve) and BzDI_{0.17}-COF

(see Figure 5A, black curve). This result suggests better ion accessibility to the electroactive center within the pore and an improvement of electron transfer of the electroactive center with the electrode material.

We have compared the electrochemical response of NDI_{0.17}-COF with those of other COFs containing NDI groups as a part of the skeleton (TAPT-NDI-COF, Figure S41) and free NDI small-molecule analogues (TAPT-NDI-A, Figure S41), reported previously by us.²⁹ Thus, NDI_{0.17}-COF (Figure S41, blue curve) presents an intermediate behavior between those of the two previously reported NDI derivatives (TAPT-NDI COF, Figure S43, black curve; and TAPT-NDI-A, Figure S43, red curve). NDI-TAPT-COF only shows a redox pair peak at $E^0 = -0.55$ V vs SCE, while NDI-TAPT-A shows two redox pairs at $E^0 = -0.80$ and $E^0 = -0.84$ V vs SCE. In the case of NDI_{0.17}-COF, all redox couples observed in NDI-TAPT-COF and NDI-TAPT-A are barely visible in its voltammogram. This behavior is a consequence of the intermediate degree of freedom of the NDI fragment in the case of NDI_{0.17}-COF, since the NDI fragment is inside the pores of the COF network. However, in the NDI-TAPT-COF, the NDI fragments are part of the COF structure, and in the NDI-TAPT-A, the NDI fragments are as free molecules.

The potential electrocatalytic effect of the modified electrodes XDI_{0.17}-COF/Carbon SuperP/GC toward the ORR was studied by analyzing their electrochemical behavior in the presence of molecular oxygen, using an O₂ saturated 0.1 M NaOH solution (Figure 5B). The catalytic currents observed in all cases demonstrate the ORR electrocatalytic effect of all XDI_{0.17}-COFs with respect to the Carbon SuperP/GC electrode ($E_{ONSET} = -0.33$ V vs SCE). Some differences are observed among them. The best electrocatalyst in terms of lower ORR onset potential and higher current intensity is NDI_{0.17}-COF, showing -0.25 V vs SCE as onset potential. A very close onset potential (-0.25 V vs SCE) is also obtained for BzDI_{0.17}-COF although the current intensity is lower. Differences in the onset potential (-0.29 V vs SCE) and in the intensity are observed for PDI_{0.17}-COF.

The electrochemical characterization for ORR electrocatalysis in static conditions has been completed using electrochemical impedance spectroscopy (EIS) for ORR electron transfer. The Nyquist plot obtained for each modified electrode (Figure 5C) clearly shows differences among the XDI_{0.17}-COF/Carbon SuperP/GC electrodes. The electron transfer of the ORR is favored in the case of NDI_{0.17}-COF ($R_p = 1.22$ k Ω) in comparison with BzDI_{0.17}-COF ($R_p = 4.91$ k Ω) and PDI_{0.17}-COF ($R_p = 7.92$ k Ω), showing in all cases less

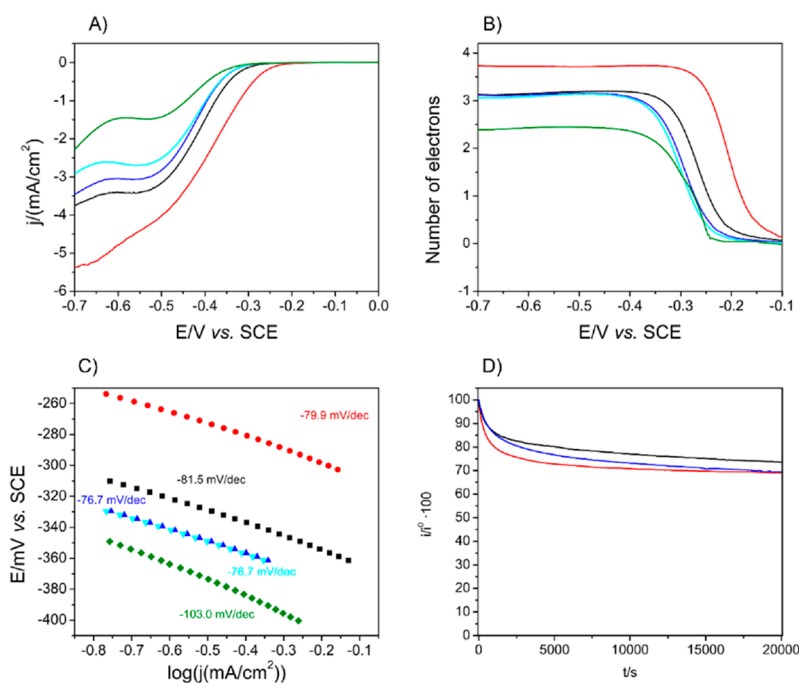


Figure 6. (A) Hydrodynamic linear sweep voltammetry and (B) number of electrons exchanged in the ORR at different potentials using RRDE of GC/Pt (disc/ring) modified with **BzDI**_{0.17}-COF/Carbon SuperP (black), **NDI**_{0.17}-COF/Carbon SuperP (red), **PDI**_{0.17}-COF/Carbon SuperP (blue), **TAPB-DMTA-COF**/Carbon SuperP (cyan), and **Carbon SuperP** (green) in an O₂ saturated 0.1 M NaOH solution at 10 mV/s and 1000 rpm. (C) Tafel slope of ORR electrocatalysis obtained from results in panel A. (D) Current intensity stability of **BzDI**_{0.17}-COF/Carbon SuperP/GC (black), **NDI**_{0.17}-COF/Carbon SuperP/GC (red), and **PDI**_{0.17}-COF/Carbon SuperP/GC (blue) electrodes operating in O₂ saturated 0.1 M NaOH solution at a constant potential (−0.4 V vs SCE).

Table 1. Summary of the Main Electrochemical Parameters of All **XDI**_{0.17}-COFs/Carbon SuperP/GC and Carbon SuperP/GC

electrode	E_{onset} vs SCE/mV	j_{lim} /(mA/cm ²)	Tafel slope/(mV/dec)	R_p /kΩ	ORR number of electrons	$\eta_{\text{experimental}}/V$	$\eta_{\text{theoretical}}/V$
NDI _{0.17} -COF/Carbon SuperP/GC	−240	−4.2	79.7	1.22	3.7	0.46	0.61
BzDI _{0.17} -COF/Carbon SuperP/GC	−290	−3.8	81.5	4.91	3.1	0.51	0.64
PDI _{0.17} -COF/Carbon SuperP/GC	−300	−3.4	76.7	7.92	3.1	0.52	0.68
TAPB-DMTA-COF	−300	−2.87	76.7	4.72	3.1	0.52	
Carbon SuperP/GC	−330	−1.51	103	8.38	2.4	0.55	

resistance for ORR electron transfer than **Carbon SuperP/GC** electrodes ($R_p = 8.38$ kΩ).

Rotating disk-ring electrodes (GC/Pt) were modified with **XDI**_{0.17}-COFs/Carbon SuperP suspensions or only with **Carbon SuperP** (used as a comparison) and employed to study the ORR in hydrodynamic conditions by linear sweep voltammetry (Figure 6A). The best results were obtained using **NDI**_{0.17}-COF/Carbon SuperP/GC ($E_{\text{ONSET}} = -0.24$ V vs SCE) and a limit current close to -4 mA/cm² compared with the **Carbon SuperP/GC** electrode ($E_{\text{ONSET}} = -0.36$ V vs SCE and $I_{\text{lim}} = -1.51$ mA/cm²). Moderate results were obtained when **BzDI**_{0.17}-COF/Carbon SuperP/GC or **PDI**_{0.17}-COF/Carbon SuperP/GC is used (in agreement with the results obtained in the static CV of Figure 5B). The number of electrons involved in the ORR was calculated from

$$n = 4 \frac{i_D}{i_D + \frac{i_R}{N}} \quad (1)$$

where n is the number of electrons, N is the collection efficiency of the ring (0.37 for the present geometrical arrangement), and i_D and i_R are the measured currents for the disk and ring electrodes, respectively. The number of

electrons exchanged during the ORR have been plotted versus the potential applied (Figure 6B). An increase in the number of electrons involved in the ORR is observed in the case of **XDI**_{0.17}-COFs/Carbon SuperP/GC electrodes, compared to **Carbon SuperP/GC** electrodes (2.4 electrons). Furthermore, when **NDI**_{0.17}-COF/Carbon SuperP/GC is employed, the number of exchanged electrons increased until 3.7, which is quite close to 4, suggesting a preference for the 4-electron ORR mechanism over the 2-electron mechanism, which is preferred for energy applications. **BzDI**_{0.17}-COF/Carbon SuperP/GC and **PDI**_{0.17}-COF/Carbon SuperP/GC electrocatalysts also increase the number of electrons exchanged during the ORR, but the increase is not so high, 3.1 electrons, suggesting a coexistence of both ORR mechanisms (2 and 4 electrons) in the same proportions. Tafel slopes have been obtained from the hydrodynamic sweep voltammograms of **XDI**_{0.17}-COFs/Carbon SuperP/GC (Figure 6C). Absolute values of Tafel slopes obtained for **XDI**_{0.17}-COFs/Carbon SuperP/GC are smaller than those obtained for **Carbon SuperP/GC** (Tafel slope = 103 mV/dec), which confirms the electrocatalytic effect of the **XDI**_{0.17}-COFs. The obtained values for **BzDI**_{0.17}-COF, **NDI**_{0.17}-COF, and **PDI**_{0.17}-COF are 76.7, 79.7, and 81.5 respectively, which are close to each other,

but are still a bit far from the Tafel slope of the 10% Pt–C/SuperP/GC electrode (68.5 mV/dec). Despite this difference, a significant reduction is obtained, pointing to more effective metal-free ORR electrocatalysts.

The stability of the XDI_{0.17}-COFs/Carbon SuperP/GC during ORR experiments has been tested applying a fixed potential of −0.4 V vs SCE for 20 ks in hydrodynamic conditions in an O₂ saturated 0.1 M NaOH solution (Figure 6D). All XDI_{0.17}-COFs/Carbon SuperP/GC electrocatalysts show similar behavior regarding stability, consisting of an initial decrease of around 20% of their initial activity during the first 200 s, and after that, the activity remains almost constant until the end of the experiment, losing only an additional 10% of the initial activity during 20 ks. We can consider that these are excellent results, taking into account the organic nature of the non-pyrolyzed metal-free electrocatalytic materials. Table 1 summarizes the main electrochemical results comparing all XDI_{0.17}-COFs/Carbon SuperP/GC and Carbon SuperP/GC. These results point out the influence of the electronic character of the moieties anchored to the COF skeleton, as well as the porosity of the final material. In this manner, structures with similar porosity values (BzDI_{0.17}-COF and NDI_{0.17}-COF) revealed the influence of the aromatic surface. Meanwhile the structure with less porous features (PDI_{0.17}-COF) led to the worst electrocatalytic behavior, showing a clear influence on the ionic accessibility to the active sites for an efficient catalytic response.

To theoretically propose a viable ORR mechanism for these systems, we have studied the ORR intermediate steps involving the adsorption of O₂, O, OH, OOH, and H₂O on the most favorable active sites within the three COF structures under study, as well as their associated free energies within the Gibbs free-energy formalism (see further details in the SI, Section S1). In a first step, in all of the structures, we have identified two favorable active sites to develop the ORR reaction on the NDI, BzDI, and PDI moieties. These two active sites are the C atoms named C₁ and C₂ in Figure 7a, with Bader point charges of +0.42 and +0.44 e[−], respectively, and the highest adsorption energies for all the intermediates, although in all three cases the most favorable is the C₂ active site over the C₁ one, with slightly stronger adsorption energies with reference to the C₁

active site. As a representative example, Figure 7b shows the optimized adsorption configurations on the C₂ site in the NDI ligand for the *O₂, *OOH, *O, and *OH ORR intermediates within the optimized NDI_{0.17}-COF. It is important to remark that the adsorption configurations of all of the ORR intermediates are very similar for all three ligands. Interestingly, there is adsorption of *O in all cases in the sense that it prefers to be adsorbed on a C₁–C₂ bridge, independently of whether the starting point of the relaxation has the O atom originally located “on-top” of a C₁ or a C₂.

According to what has been presented in this paper, we have investigated the ORR catalytic performance, involving four-electron transfer steps, for the C₂ active site in all of the COF structures. Free energy diagrams constructed for the XDI_{0.17}-COFs are shown in Figure 8 at 298.15 K and pH = 0 at different electrode potentials ($U = 0$ V, working potential in each case and 1.23 V). As expected, all of the three free-energy reactions are downhill at $U = 0$ V, which indicates that thermodynamically the four-electron reaction pathway is clearly favorable. For the NDI_{0.17}-COF and the PDI_{0.17}-COF, the potential determining step is the formation of the second H₂O molecule, while for BzDI_{0.17}-COF the determining reaction step is the formation of *OH from *O. From the theoretical analysis, among the three compounds studied, the NDI_{0.17}-COF manifests the highest ORR catalytic activity on account of its highest working potential of 0.62 eV, which yields an ORR overpotential of $\eta_{\text{ORR}} = 0.61$ V. BzDI_{0.17}-COF and PDI_{0.17}-COF exhibit a slightly poorer, although also good, catalytic activity with working potentials of 0.59 and 0.55 V, and associated ORR overpotentials of 0.64 and 0.68 V, respectively. At this point, it is worth mentioning that these results accurately resemble the experimentally observed ORR catalytic performances, with the NDI_{0.17}-COF being the best candidate, followed in efficiency by BzDI_{0.17}-COF and PDI_{0.17}-COF, respectively (Table 1).

As a proof of concept, in an attempt to rationalize the origin of the small differences in the η_{ORR} of the different COFs, and since within this kind of COF system the electronic properties of the molecular building blocks remain almost unaltered with reference to their molecular states, we have computed different electronic properties of the NDI, BzDI, and PDI molecular systems (neutral, anion, and cation forms) in order to establish a correlation with the obtained η_{ORR} values of 0.61, 0.64, and 0.68 V (see details of these calculations in the SI), respectively. Since the ORR catalytic mechanism involves the sequential capture of 4 electrons, we have calculated the adiabatic electronic affinities (AEAs) of the molecular systems to check which system is able to accommodate electrons in a more efficient way. As a result of these new calculations, we have obtained values for adiabatic electronic affinities for the NDI, BzDI, and PDI molecular systems of −2.57, −2.26, and −1.92 eV, respectively, which correlate with the obtained η_{ORR} values, in the sense that the higher energy release and the more optimal stabilization toward the gain of electrons are observed for the NDI with an AEA value of −2.57 eV, being the system with the best theoretical catalytic performance with a theoretical η_{ORR} of 0.61 V. This rationalization is also consistent by the correlation between AEAs of −2.26 and −1.92 eV and η_{ORR} of 0.64 and 0.68 V for BzDI and PDI, respectively.

Interestingly, the experimental overpotentials are lower than their theoretical counterparts which were calculated for isolated molecules, with a constant difference around 0.15 V

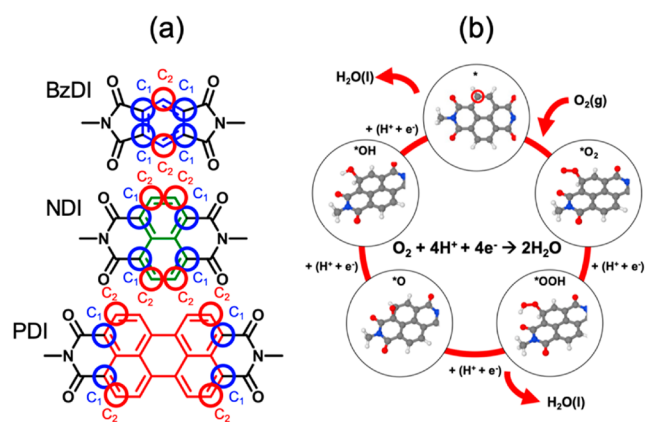


Figure 7. (a) Active ORR sites detected within the NDI, BzDI and PDI moieties by DFT-based calculations named C₁ (blue circles) and C₂ (red circles). (b) Optimized adsorption configurations for the most active C₂ site in the NDI ligand for the *O₂, *OOH, *O, and *OH ORR intermediates within the optimized NDI_{0.17}-COF. These adsorption configurations are essentially the same for all three ligands.

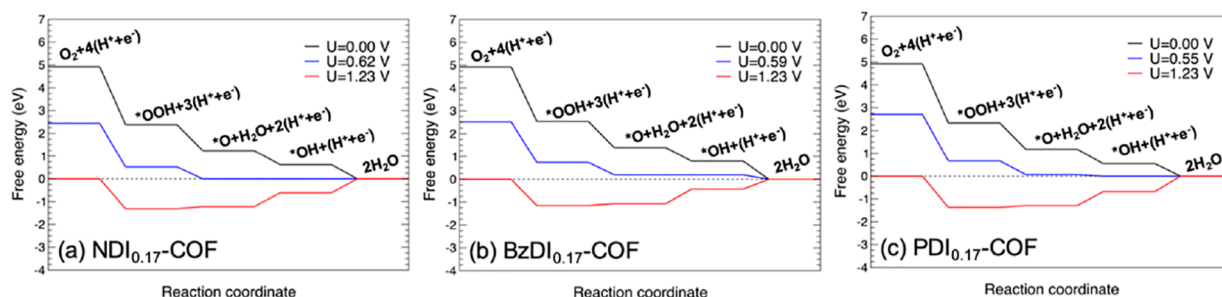


Figure 8. Free energy change of the ORR at 298.15 K and pH = 0 for the best-performing C₂ active site on (a) NDI_{0.17}-COF, (b) BzDI_{0.17}-COF, and (c) PDI_{0.17}-COF at different electrode potentials. The calculated working potential is indicated by the blue line, being the potential for which the first reaction step becomes downhill with reference to the rest of the steps. The ORR overpotential for each case, yielding the ORR catalytic performance, can be easily obtained as the difference between the fuel cell potential of 1.23 V minus the working potential for each COF system.

for all of the products. These results suggest that there is a cooperativity effect between components of the XDI_{0.17}-COFs/Carbon SuperP/GC composites toward the oxygen electroreduction which is not considered in DFT calculations. However, the constant difference between the theoretical and experimental overpotential values means that the theoretical calculations reveal evidence in the ORR mechanism and provide powerful information for the NDI modification to enhance the electrocatalytic response by chemical modulation of this active center.

CONCLUSIONS

In summary, we have developed a new strategy to evaluate the performance of organic molecules as metal-free and non-pyrolyzed electrocatalysts. This work facilitates the evaluation of novel active sites by the covalently anchoring by click chemistry in crystalline and porous networks which prevents the active site agglomeration, increases the surface–volume ratio, and ensures a close contact with electrodes. To demonstrate this, a family of electroactive diimide-based XDI_{0.17}-COFs by the postsynthetic modification of the novel Azide_{0.17}-COF were carried out by varying the “X” aromatic surface between the diimide functional groups from benzene to perylene with a molar loading of 7.65×10^{-4} mol of active site/mg of host COF. These XDI_{0.17}-COFs retain the crystalline features of the parent Azide_{0.17}-COF with a hexagonal eclipsed stacking of the network, locating the XDI units embedded inside the COF cavities and covalently anchored to the pore walls. Dispersion of these compounds by LPE produced XDI_{0.17}-COFs colloids which can be used for glassy carbon electrode modification by drop-casting. Electrochemical studies revealed that the most convenient moiety under study, for energy-related applications, was the NDI_{0.17}-COF through the 4-electron pathway with an onset potential of 0.77 V (vs RHE) and a limiting current of 4.2 mA/cm². DFT theoretical calculations were used to evaluate the ORR mechanism, confirming that the naphthalenediimide moieties show the best performance toward the oxygen electroreduction. It is also worth pointing out that a comparison between the ORR electrocatalytic performance of NDI_{0.17}-COF with those of other non-pyrolyzed and metal-free COF-based electrocatalysts (Table S2) reveals comparable results in terms of onset potential and current density in addition to the easier access to crystalline porous COFs offered by the click chemistry postfunctionalization methodology. Despite the fact that these results are still far from those offered by other derived carbons produced by pyrolytic treatment of

organic precursors (Table S3), we envisage that this easy strategy, avoiding de novo synthesis, could accelerate the discovery of novel nonpyrolyzed and metal-free COF-based electrocatalysts.

ASSOCIATED CONTENT

Supporting Information

The Supporting Information is available free of charge at <https://pubs.acs.org/doi/10.1021/acssuschemeng.2c05826>.

Materials and methods; COF characterization by PXRD, FTIR, ¹³C-CP-MAS NMR, N₂ sorption isotherms, TGA SEM, TEM, and DLS; additional electrochemical measurements; and experimental procedures (PDF)

Crystallographic Information File for Azide_{0.17}-COF (CIF)

Crystallographic Information File for BzDI_{0.17}-COF (CIF)

Crystallographic Information File for NDI_{0.17}-COF (CIF)

Crystallographic Information File for PDI_{0.17}-COF (CIF)

AUTHOR INFORMATION

Corresponding Authors

José L. Segura – Departamento de Química Orgánica I, Facultad de CC. Químicas, Universidad Complutense de Madrid, 28040 Madrid, Spain; orcid.org/0000-0002-3360-1019; Email: segura@ucm.es

Encarnación Lorenzo – Departamento de Química Analítica y Análisis Instrumental, Facultad de Ciencias, Universidad Autónoma de Madrid, 28049 Madrid, Spain; Instituto Madrileño de Estudios Avanzados en Nanociencia (IMDEA-Nanociencia), 28049 Madrid, Spain; Institute for Advanced Research in Chemical Sciences (IAdChem), Universidad Autónoma de Madrid, 28049 Madrid, Spain; orcid.org/0000-0001-8432-9652; Email: encarnacion.lorenzo@uam.es

Authors

Marcos Martínez-Fernández – Departamento de Química Orgánica I, Facultad de CC. Químicas, Universidad Complutense de Madrid, 28040 Madrid, Spain

Emiliano Martínez-Periñán – Departamento de Química Analítica y Análisis Instrumental, Facultad de Ciencias, Universidad Autónoma de Madrid, 28049 Madrid, Spain; Institute for Advanced Research in Chemical Sciences

(IAdChem), Universidad Autónoma de Madrid, 28049 Madrid, Spain

José I. Martínez – Departamento de Nanoestructuras, Superficies, Recubrimientos y Astrofísica Molecular, Instituto de Ciencia de Materiales de Madrid (ICMM-CSIC), 28049 Madrid, Spain

Marta Gordo-Lozano – Departamento de Química Orgánica I, Facultad de CC. Químicas, Universidad Complutense de Madrid, 28040 Madrid, Spain; orcid.org/0000-0002-2764-6157

Félix Zamora – Departamento de Química Inorgánica, Facultad de Ciencias, Institute for Advanced Research in Chemical Sciences (IAdChem), and Condensed Matter Physics Center (IFIMAC), Universidad Autónoma de Madrid, 28049 Madrid, Spain; Instituto Madrileño de Estudios Avanzados en Nanociencia (IMDEA-Nanociencia), 28049 Madrid, Spain; orcid.org/0000-0001-7529-5120

Complete contact information is available at:

<https://pubs.acs.org/10.1021/acssuschemeng.2c05826>

Author Contributions

○M.M.-F. and E.M.-P. contributed equally. M.M.-F.: Investigation, Data curation, Visualization, Writing—original draft, Writing—review and editing. E.M.-P.: Investigation, Data curation, Visualization, Writing—original draft, Writing—review and editing. J.I.M.: Conceptualization, Investigation, Data curation, Visualization, Writing—original draft, Writing—review and editing. M.G.-L.: Investigation, Data curation, Writing—original draft, Writing—review and editing. F.Z.: Conceptualization, Investigation, Visualization, Writing—review and editing. J.L.S.: Conceptualization, Investigation, Visualization, Supervision, Writing—review and editing, Funding acquisition, Project administration. E.L.: Conceptualization, Investigation, Visualization, Supervision, Writing—review and editing, Funding acquisition, Project administration.

Funding

This work was financially supported by Ministerio de Ciencia e Innovación of Spain MICINN (TED2021-129886B-C43; PID2019-106268GB-C33; RED2018-102412-T; PID2020-116728RB-I00; PID2019-106268GB-C32; Grants PID2020-113142RB-C21 and PLEC2021-007906; funded MCIN/AEI/10.13039/501100011033), Comunidad de Madrid (P2018/NMT-4349 TRANSNANOAVANSENS Program; SI3/PJI/2021-00341, Grants S2018/NMT-4367 and Y2020/NMT6469), and the UCM (INV.GR.00.1819.10759).

Notes

The authors declare no competing financial interest.

REFERENCES

- (1) Ma, R.; Lin, G.; Zhou, Y.; Liu, Q.; Zhang, T.; Shan, G.; Yang, M.; Wang, J. A review of oxygen reduction mechanisms for metal-free carbon-based electrocatalysts. *npj Computational Materials* **2019**, *5* (1), 78.
- (2) Gewirth, A. A.; Varnell, J. A.; DiAscro, A. M. Nonprecious Metal Catalysts for Oxygen Reduction in Heterogeneous Aqueous Systems. *Chem. Rev.* **2018**, *118* (5), 2313–2339.
- (3) Shao, M.; Chang, Q.; Dodelet, J.-P.; Chenitz, R. Recent Advances in Electrocatalysts for Oxygen Reduction Reaction. *Chem. Rev.* **2016**, *116* (6), 3594–3657.
- (4) Wagner, F. T.; Lakshmanan, B.; Mathias, M. F. Electrochemistry and the Future of the Automobile. *J. Phys. Chem. Lett.* **2010**, *1* (14), 2204–2219.

- (5) Grumelli, D.; Wurster, B.; Stepanow, S.; Kern, K. Bio-inspired nanocatalysts for the oxygen reduction reaction. *Nat. Commun.* **2013**, *4* (1), 2904.
- (6) Di Noto, V.; Pagot, G.; Negro, E.; Vezzù, K.; Kulesza, P. J.; Rutkowska, I. A.; Pace, G. A formalism to compare electrocatalysts for the oxygen reduction reaction by cyclic voltammetry with the thin-film rotating ring-disk electrode measurements. *Current Opinion in Electrochemistry* **2022**, *31*, 100839.
- (7) Li, D.; Li, C.; Zhang, L.; Li, H.; Zhu, L.; Yang, D.; Fang, Q.; Qiu, S.; Yao, X. Metal-Free Thiophene-Sulfur Covalent Organic Frameworks: Precise and Controllable Synthesis of Catalytic Active Sites for Oxygen Reduction. *J. Am. Chem. Soc.* **2020**, *142* (18), 8104–8108.
- (8) Bajracharya, S.; ElMekawy, A.; Srikanth, S.; Pant, D. Cathodes for microbial fuel cells. In *Microbial Electrochemical and Fuel Cells*; Scott, K., Yu, E. H., Eds.; Woodhead Publishing: Boston, 2016; Chapter 6, pp 179–213.
- (9) Wang, N.; Ma, S.; Zuo, P.; Duan, J.; Hou, B. Recent Progress of Electrochemical Production of Hydrogen Peroxide by Two-Electron Oxygen Reduction Reaction. *Advanced Science* **2021**, *8* (15), 2100076.
- (10) Debe, M. K. Electrocatalyst approaches and challenges for automotive fuel cells. *Nature* **2012**, *486* (7401), 43–51.
- (11) Wang, M.; Wang, C.; Liu, J.; Rong, F.; He, L.; Lou, Y.; Zhang, Z.; Du, M. Efficient Ag/Ag₂O-Doped Cobalt Metallo-Covalent Organic Framework Electrocatalysts for Rechargeable Zinc-Air Battery. *ACS Sustainable Chem. Eng.* **2021**, *9* (17), 5872–5883.
- (12) Yang, Y.; Lu, Y.; Zhang, H.-Y.; Wang, Y.; Tang, H.-L.; Sun, X.-J.; Zhang, G.; Zhang, F.-M. Decoration of Active Sites in Covalent Organic Framework: An Effective Strategy of Building Efficient Photocatalysis for CO₂ Reduction. *ACS Sustainable Chem. Eng.* **2021**, *9* (39), 13376–13384.
- (13) Yang, C.; Tao, S.; Huang, N.; Zhang, X.; Duan, J.; Makiura, R.; Maenosono, S. Heteroatom-Doped Carbon Electrocatalysts Derived from Nanoporous Two-Dimensional Covalent Organic Frameworks for Oxygen Reduction and Hydrogen Evolution. *ACS Applied Nano Materials* **2020**, *3* (6), 5481–5488.
- (14) Xu, Q.; Tang, Y.; Zhang, X.; Oshima, Y.; Chen, Q.; Jiang, D. Template Conversion of Covalent Organic Frameworks into 2D Conducting Nanocarbons for Catalyzing Oxygen Reduction Reaction. *Adv. Mater.* **2018**, *30* (15), 1706330.
- (15) Zhou, N.; Wang, N.; Wu, Z.; Li, L. Probing Active Sites on Metal-Free, Nitrogen-Doped Carbons for Oxygen Electroreduction: A Review. *Catalysts* **2018**, *8* (11), 509.
- (16) Yan, X.; Wang, B.; Ren, J.; Long, X.; Yang, D. An Unsaturated Bond Strategy to Regulate Active Centers of Metal-Free Covalent Organic Frameworks for Efficient Oxygen Reduction. *Angew. Chem., Int. Ed.* **2022**, *61* (46), e202209583.
- (17) Xu, Q.; Qian, J.; Luo, D.; Liu, G.; Guo, Y.; Zeng, G. Ni/Fe Clusters and Nanoparticles Confined by Covalent Organic Framework Derived Carbon as Highly Active Catalysts toward Oxygen Reduction Reaction and Oxygen Evolution Reaction. *Advanced Sustainable Systems* **2020**, *4* (9), 2000115.
- (18) Zhang, J.; Zhang, G.; Jin, S.; Zhou, Y.; Ji, Q.; Lan, H.; Liu, H.; Qu, J. Graphitic N in nitrogen-Doped carbon promotes hydrogen peroxide synthesis from electrocatalytic oxygen reduction. *Carbon* **2020**, *163*, 154–161.
- (19) Segura, J. L.; Royuela, S.; Mar Ramos, M. Post-synthetic modification of covalent organic frameworks. *Chem. Soc. Rev.* **2019**, *48* (14), 3903–3945.
- (20) Gomes, R.; Bhattacharyya, A. J. Carbon Nanotube-Templated Covalent Organic Framework Nanosheets as an Efficient Sulfur Host for Room-Temperature Metal-Sulfur Batteries. *ACS Sustainable Chem. Eng.* **2020**, *8* (15), 5946–5953.
- (21) Yang, S.; Li, T.; Cheng, Y.; Fan, W.; Wang, L.; Liu, Y.; Bian, L.; Zhou, C.-H.; Zheng, L.-Y.; Cao, Q.-E. Covalent Organic Framework Isomers for Photoenhanced Gold Recovery from E-Waste with High Efficiency and Selectivity. *ACS Sustainable Chem. Eng.* **2022**, *10* (30), 9719–9731.
- (22) Huang, Y.; Kong, F.; Tian, H.; Pei, F.; Chen, Y.; Meng, G.; Chang, Z.; Chen, C.; Cui, X.; Shi, J. Ultrauniformly Dispersed Cu

Nanoparticles Embedded in N-Doped Carbon as a Robust Oxygen Electrocatalyst. *ACS Sustainable Chem. Eng.* **2022**, *10* (19), 6370–6381.

(23) Zhang, H.; Zhu, M.; Schmidt, O. G.; Chen, S.; Zhang, K. Covalent Organic Frameworks for Efficient Energy Electrocatalysis: Rational Design and Progress. *Advanced Energy and Sustainability Research* **2021**, *2* (4), 2000090.

(24) Zhao, X.; Pachfule, P.; Thomas, A. Covalent organic frameworks (COFs) for electrochemical applications. *Chem. Soc. Rev.* **2021**, *50* (12), 6871–6913.

(25) Haase, F.; Lotsch, B. V. Solving the COF trilemma: towards crystalline, stable and functional covalent organic frameworks. *Chem. Soc. Rev.* **2020**, *49* (23), 8469–8500.

(26) Chang, S.; Li, C.; Li, H.; Zhu, L.; Fang, Q. Stable Thiophene-sulfur Covalent Organic Frameworks for Oxygen Reduction Reaction- (ORR). *Chemical Research in Chinese Universities* **2022**, *38* (2), 396–401.

(27) Wu, S.; Li, M.; Phan, H.; Wang, D.; Herng, T. S.; Ding, J.; Lu, Z.; Wu, J. Toward Two-Dimensional π -Conjugated Covalent Organic Radical Frameworks. *Angew. Chem., Int. Ed.* **2018**, *57* (27), 8007–8011.

(28) García-Arroyo, P.; Martínez-Periñán, E.; Cabrera-Trujillo, J. J.; Salagre, E.; Michel, E. G.; Martínez, J. I.; Lorenzo, E.; Segura, J. L. Pyrenetetraone-based covalent organic framework as an effective electrocatalyst for oxygen reduction reaction. *Nano Research* **2022**, *15* (5), 3907–3912.

(29) Martínez-Fernández, M.; Martínez-Periñán, E.; Royuela, S.; Martínez, J. I.; Zamora, F.; Lorenzo, E.; Segura, J. L. Covalent organic frameworks based on electroactive naphthalenediimide as active electrocatalysts toward oxygen reduction reaction. *Applied Materials Today* **2022**, *26*, 101384.

(30) Royuela, S.; Martínez-Periñán, E.; Arrieta, M. P.; Martínez, J. I.; Ramos, M. M.; Zamora, F.; Lorenzo, E.; Segura, J. L. Oxygen reduction using a metal-free naphthalene diimide-based covalent organic framework electrocatalyst. *Chem. Commun.* **2020**, *56* (8), 1267–1270.

(31) Li, Q.; Zhang, S.; Dai, L.; Li, L.-s. Nitrogen-Doped Colloidal Graphene Quantum Dots and Their Size-Dependent Electrocatalytic Activity for the Oxygen Reduction Reaction. *J. Am. Chem. Soc.* **2012**, *134* (46), 18932–18935.

(32) Liu, X.; Hu, M.; Wang, M.; Song, Y.; Zhou, N.; He, L.; Zhang, Z. Novel nanoarchitecture of Co-MOF-on-TPN-COF hybrid: Ultra-lowly sensitive bioplatfrom of electrochemical aptasensor toward ampicillin. *Biosens. Bioelectron.* **2019**, *123*, 59–68.

(33) Li, H.; Kou, B.; Yuan, Y.; Chai, Y.; Yuan, R. Porous Fe₃O₄@COF-Immobilized gold nanoparticles with excellent catalytic performance for sensitive electrochemical detection of ATP. *Biosens. Bioelectron.* **2022**, *197*, 113758.

(34) Yan, T.; Lan, Y.; Tong, M.; Zhong, C. Screening and Design of Covalent Organic Framework Membranes for CO₂/CH₄ Separation. *ACS Sustainable Chem. Eng.* **2019**, *7* (1), 1220–1227.

(35) Xu, H.; Gao, J.; Jiang, D. Stable, crystalline, porous, covalent organic frameworks as a platform for chiral organocatalysts. *Nat. Chem.* **2015**, *7* (11), 905–912.

(36) Chen, L.; Furukawa, K.; Gao, J.; Nagai, A.; Nakamura, T.; Dong, Y.; Jiang, D. Photoelectric Covalent Organic Frameworks: Converting Open Lattices into Ordered Donor-Acceptor Heterojunctions. *J. Am. Chem. Soc.* **2014**, *136* (28), 9806–9809.

(37) Ji, W.; Xiao, L.; Ling, Y.; Ching, C.; Matsumoto, M.; Bisbey, R. P.; Helbling, D. E.; Dichtel, W. R. Removal of GenX and Perfluorinated Alkyl Substances from Water by Amine-Functionalized Covalent Organic Frameworks. *J. Am. Chem. Soc.* **2018**, *140* (40), 12677–12681.

(38) Xu, Q.; Tao, S.; Jiang, Q.; Jiang, D. Designing Covalent Organic Frameworks with a Tailored Ionic Interface for Ion Transport across One-Dimensional Channels. *Angew. Chem., Int. Ed.* **2020**, *59* (11), 4557–4563.

(39) Martín-Illán, J. Á.; Rodríguez-San-Miguel, D.; Castillo, O.; Beobide, G.; Perez-Carvajal, J.; Imaz, I.; Maspoch, D.; Zamora, F.

Macroscopic Ultralight Aerogel Monoliths of Imine-based Covalent Organic Frameworks. *Angew. Chem., Int. Ed.* **2021**, *60* (25), 13969–13977.

(40) Xu, Q.; Tao, S.; Jiang, Q.; Jiang, D. Ion Conduction in Polyelectrolyte Covalent Organic Frameworks. *J. Am. Chem. Soc.* **2018**, *140* (24), 7429–7432.

(41) Frisch, M. J.; Trucks, G. W.; Schlegel, H. B.; Scuseria, G. E.; Robb, M. A.; Cheeseman, J. R.; Scalmani, G.; Barone, V.; Petersson, G. A.; Nakatsuji, H.; Li, X.; Caricato, M.; Marenich, A. V.; Bloino, J.; Janesko, B. G.; Gomperts, R.; Mennucci, B.; Hratchian, H. P.; Ortiz, J. V.; Izmaylov, A. F.; Sonnenberg, J. L.; Williams-Young, D.; Ding, F.; Lipparini, F.; Egidi, F.; Goings, J.; Peng, B.; Petrone, A.; Henderson, T.; Ranasinghe, D.; Zakrzewski, V. G.; Gao, J.; Rega, N.; Zheng, G.; Liang, W.; Hada, M.; Ehara, M.; Toyota, K.; Fukuda, R.; Hasegawa, J.; Ishida, M.; Nakajima, T.; Honda, Y.; Kitao, O.; Nakai, H.; Vreven, T.; Throssell, K.; Montgomery, J. A., Jr.; Peralta, J. E.; Ogliaro, F.; Bearpark, M.; Heyd, J. J.; Brothers, E. N.; Kudin, K. N.; Staroverov, V. N.; Kobayashi, R.; Normand, J.; Raghavachari, K.; Rendell, A.; Burant, J. C.; Iyengar, S. S.; Tomasi, J.; Cossi, M.; Millam, J. M.; Klene, M.; Adamo, C.; Cammi, R.; Ochterski, J. W.; Martin, R. L.; Morokuma, K.; Farkas, O.; Foresman, J. B.; Fox, D. J. *Gaussian 16*, revision C.01; Gaussian, Inc.: Wallingford CT, 2016.

(42) Giannozzi, P.; Baroni, S.; Bonini, N.; Calandra, M.; Car, R.; Cavazzoni, C.; Ceresoli, D.; Chiarotti, G. L.; Cococcioni, M.; Dabo, I.; Dal Corso, A.; de Gironcoli, S.; Fabris, S.; Fratesi, G.; Gebauer, R.; Gerstmann, U.; Gougoussis, C.; Kokalj, A.; Lazzeri, M.; Martin-Samos, L.; Marzari, N.; Mauri, F.; Mazzarello, R.; Paolini, S.; Pasquarello, A.; Paulatto, L.; Sbraccia, C.; Scandolo, S.; Sclauzero, G.; Seitsonen, A. P.; Smogunov, A.; Umari, P.; Wentzcovitch, R. M. QUANTUM ESPRESSO: a modular and open-source software project for quantum simulations of materials. *J. Phys.: Condens. Matter* **2009**, *21* (39), 395502.

(43) Toby, B. H.; Von Dreele, R. B. GSAS-II: the genesis of a modern open-source all purpose crystallography software package. *J. Appl. Crystallogr.* **2013**, *46* (2), S44–S49.

(44) Royuela, S.; Gil-San Millán, R.; Mancheño, M. J.; Ramos, M. M.; Segura, J. L.; Navarro, J. A. R.; Zamora, F. Catalytically Active Imine-based Covalent Organic Frameworks for Detoxification of Nerve Agent Simulants in Aqueous Media. *Materials* **2019**, *12* (12), 1974.

(45) Mu, Z.-J.; Ding, X.; Chen, Z.-Y.; Han, B.-H. Zwitterionic Covalent Organic Frameworks as Catalysts for Hierarchical Reduction of CO₂ with Amine and Hydrosilane. *ACS Appl. Mater. Interfaces* **2018**, *10* (48), 41350–41358.

(46) Adel, R.; Gala, E.; Alonso-Navarro, M. J.; Gutierrez-Fernandez, E.; Martín, J.; Stella, M.; Martínez-Ferrero, E.; de la Peña, A.; Harbuzaru, A.; Ramos, M. M.; Ortiz, R. P.; Segura, J. L.; Campoy-Quiles, M. Comparing the microstructure and photovoltaic performance of 3 perylene imide acceptors with similar energy levels but different packing tendencies. *Journal of Materials Chemistry C* **2022**, *10* (5), 1698–1710.

(47) Cui, W.-R.; Zhang, C.-R.; Jiang, W.; Liang, R.-P.; Wen, S.-H.; Peng, D.; Qiu, J.-D. Covalent Organic Framework Nanosheet-Based Ultrasensitive and Selective Colorimetric Sensor for Trace Hg²⁺ Detection. *ACS Sustainable Chem. Eng.* **2019**, *7* (10), 9408–9415.

(48) Wu, X.; Qi, Y.; Hong, J. J.; Li, Z.; Hernandez, A. S.; Ji, X. Rocking-Chair Ammonium-Ion Battery: A Highly Reversible Aqueous Energy Storage System. *Angew. Chem., Int. Ed.* **2017**, *56* (42), 13026–13030.

(49) Tsai, H.-H.; Lin, T.-J.; Vedhanarayanan, B.; Tsai, C.-C.; Chen, T.-Y.; Ji, X.; Lin, T.-W. A 1.9-V all-organic battery-supercapacitor hybrid device with high rate capability and wide temperature tolerance in a metal-free water-in-salteelectrolyte. *J. Colloid Interface Sci.* **2022**, *612*, 76–87.